Journal of Mechanical Science and Technology 32 (8) (2018) 3817~3834
www.springerlink.com/content/1738-494x(Print)/1976-3824(Online)
DOI 10.1007/s12206-018-0734-3

Research on force and temperature characteristics of novel point grinding wheels[†]

G. Q. Yin*, Y. D. Gong, Y. W. Li and J. Cheng

School of Mechanical Engineering and Automation, Northeastern University, Shenyang, 110819, China

(Manuscript Received January 23, 2018; Revised April 13, 2018; Accepted April 17, 2018)

Abstract

We propose a novel point grinding wheel (NPGW) with coarse grinding zone angle θ. According to earlier studies, this type of grinding wheel has high grinding efficiency, long service life, and generates very little surface roughness. The contact zone between the grinding wheel and workpiece is modified by the addition of the NPGW with the coarse grinding zone angle θ and the inclined angle α of point grinding process, and as a result, grinding force and grinding zone temperature are also altered. The grinding force theoretical model of NPGW was established and the grinding zone temperature was simulated by the finite element method, based on the theory of grinding heat generation and distribution and triangular heat source distribution model. At the same time, seven pieces of NPGW with different angles θ used for grinding experiments were fabricated. The theoretical model of grinding force and the simulation of grinding temperature coincided with experimental results. Therefore, the grinding force theoretical model and the grinding temperature simulation provide an auxiliary and predictive method for the actual process. Moreover, the influence of parameters on grinding force and grinding zone temperature can be obtained, and the results indicate that the NPGW and point grinding process can reduce grinding force and grinding zone temperature. Finally, plastic deformation is attributed to the production of compressive stress and grinding heat is attributed to the production of tensile stress. Therefore, the residual stress is influenced by the grinding force and the grinding temperature coupled. The residual stress of workpiece surface and subsurface was studied. In conclusion, the NPGW and point grinding process can reduce residual stress of workpiece surface and subsurface, in the case of tensile and compressive stress.

Keywords: Novel point grinding wheel; Point grinding; Grinding force; Grinding temperature; Residual stress

---

1. Introduction

In comparison to traditional cylindrical grinding, the grinding wheel axis is not parallel to the workpiece axis, but there is an angle between the grinding wheel axis and workpiece axis in the point grinding process. Typically, the angle is called inclining angle α. As a result of the inclining angle α, the contact between grinding wheel and workpiece changes from a line contact to point contact [1], as shown in Fig. 1. Thus the wheel-workpiece contact zone is reduced, the machining accuracy and surface quality of workpiece are improved [2], and the grinding force is also changed.

Many factors all have a relationship with grinding force, such as wheel wear, the dynamic characteristics of manufacturing equipment, geometric accuracy and surface quality of the workpiece [3]. Therefore, many researchers have focused on the computing of the grinding force and have made considerable progress. Badger and Torrance [4] proposed a grinding force model to simulate a rigid plastic contact of the grain and the workpiece. It was said that the slope of grains and the friction coefficient of the contact surface would affect the mechanical properties of such contact. Hecker [5] put forward another grinding force model, within which the grinding thickness was distributed according to Riley probability density distribution and kinematic conditions, material properties, wheel microstructure and other dynamic effects took taken into account the probability density function.

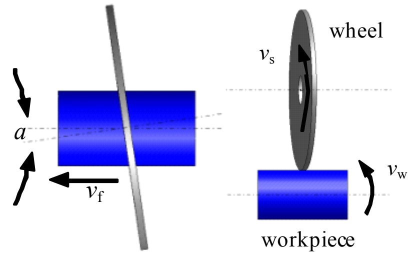

Fig. 1. Schematic of point grinding.

During the grinding process, very high energy is fed into the removed unit volume metal, and almost all energy conversion is concentrated in the grinding zone. Service life and grinding accuracy of grinding wheel are influenced by the large amount of grinding heat in grinding zone [6]. The residual stress can

---

*Corresponding author. Tel.: +86 13897958957, Fax.: +86 24 83678667
E-mail address: yinguoqiang@me.neu.edu.cn

[†] Recommended by Associate Editor Yongho Jeon

be influenced by the grinding force and the grinding temperature coupled. Therefore, residual stress can simultaneously reflect grinding force and grinding heat during the grinding process.

In recent years, grinding temperature and residual stress have also been studied. Santander [7] established a heat transfer model for grinding workpiece surface assuming a constant heat transfer coefficient for the coolant acting on the workpiece surface and simulated the temperature field of linear heat flux profiles in the stationary regime. The results proved that the maximum temperature was located in the grinding zone on the surface, and converted the search of the maximum temperature in a three-dimensional temperature field within an unbounded region into the search of the maximum for a one-dimensional function within a particular interval. The method of temperature assessment in surface grinding of tool steels was studied by Rao and Vinay [8]. A mathematical model was established to evaluate the temperature generated and then simulation was carried out. They concluded that the mathematical model, simulation and experimental results were consistent. The temperature recorded at medium feed rate as well as medium cutting depth was appropriate and higher dressing depth was better than the lower one for reducing the temperature during surface grinding. Rowe [9] studied the thermal characteristics of high efficiency deep grinding (HEDG) and provided a method for order of magnitude estimation of temperatures. It was concluded that with high wheel speed, energy analysis suggested it is possible to tolerate workpiece temperature approaching the melting temperature of the workpiece material with potential benefits of reduced energy consumption, reduced grinding forces and reduced damage to the finished workpiece surface. Huang [10] studied the residual stress in the grinding surface of superalloys and iron alloys. By using regression analysis, the relation formula between the grinding surface residual stress and the grinding factors, and the influence of grinding parameters on residual stress were obtained. Sun [11] established a 3D finite element model and simulated cutting process for Al2A12, and residual stress on the machined surface was predicted and calculated. The simulation results coincided with the experimental results, and the influence of processing parameters on the residual stress was obtained.

Despite the grinding force model and the grinding temperature extensively studied by researchers, most of them are only applied for traditional grinding, and little for point grinding, especially the NPGW with coarse grinding zone angle θ. Furthermore, the contact zone of point grinding is small and the heat transmission is fast, which makes it more difficult to measure the grinding temperature. Therefore, a new theory is needed for predicting the effect of grinding parameters on the grinding force and the grinding temperature of NPGW. The NPGW can take into account both coarse grinding zone and precision grinding zone, which makes these two stages orderly, reduces wear and improves the machining precision and machining efficiency [12]. The residual stress of workpiece surface and subsurface is studied deeply, because it can simultaneously reflect the effect of grinding force and grinding heat in grinding process.

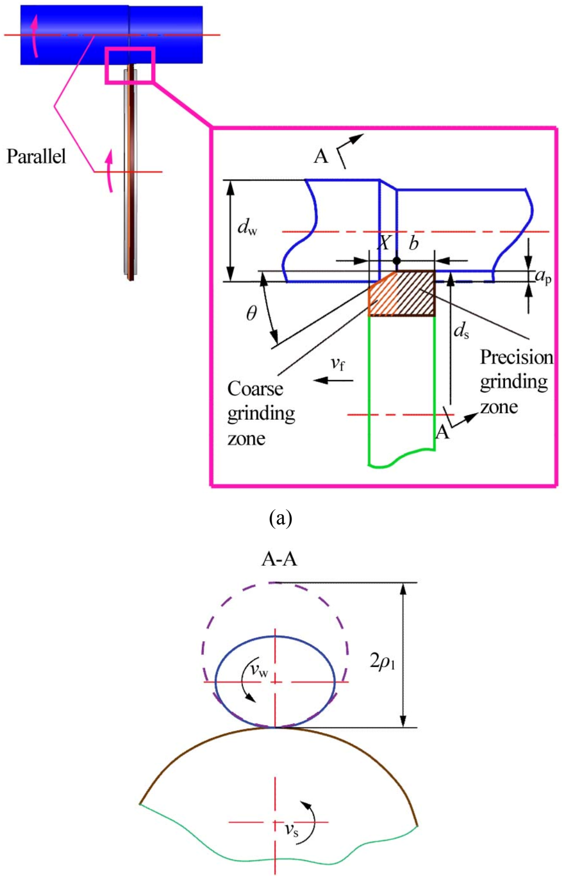

(a)

(b)

Fig. 2. Schematic of traditional grinding with NPGW.

2. The theory of point grinding force and temperature with NPGW

2.1 The grinding force theoretical model of NPGW

2.1.1 The geometry model in traditional processing with NPGW

The NPGW has a coarse grinding zone angle θ in the front part of the abrasive layer. The processing schematic of this grinding wheel is shown in Fig. 2(a). The wheel-workpiece contact zone can be divided into coarse grinding zone on the left side and precision grinding zone on the right side. Coarse grinding zone in the front part is mainly used to remove the materials, which determines the grinding efficiency. Precision grinding zone is used to remove the remaining materials to meet the requirements of the workpiece size and do finishing for processed surface, which has influence on grinding precision [12].

In traditional cylindrical processing, the axis of the grinding wheel is parallel to workpiece axis as shown in Fig. 2(a). While, the grinding wheel and workpiece are elliptical in vertical direction of contact surface projection as shown in Fig. 2(b) A-A direction. The elliptical workpiece and grinding wheel are equivalent to circles. The equivalent diameter and equivalent velocity of the workpiece and grinding wheel in A-A direction can be calculated using the radius of curvature of the workpiece ρ_1 at the contact point.

$$\begin{cases} d_{we1} = 2\rho_1 = \dfrac{d_w^{\ 2}}{d_w \cos\theta} = \dfrac{d_w}{\cos\theta} \\ d_{se1} = \dfrac{d_s^{\ 2}}{d_s \cos\theta} = \dfrac{d_s}{\cos\theta} \end{cases} \tag{1}$$

$$\begin{cases} v_{we1} = v_w \\ v_{se1} = v_s \end{cases} \tag{2}$$

where d_w and d_s are the diameters of the workpiece and grinding wheel, d_{we1} and d_{se1} are the equivalent diameters of the workpiece and grinding wheel in traditional processing with NPGW, v_{w} and v_{s} are the speed of the workpiece and grinding wheel, v_{we1} and v_{se1} are the equivalent speed of the workpiece and grinding wheel in traditional processing with NPGW.

The equivalent wheel diameter in traditional processing with NPGW d_{e1} is,

$$d_{e1} = \frac{d_{se1}}{1 + d_{se1} / d_{we1}} = \frac{d_s d_w}{\cos\theta\left(d_s + d_w\right)} . \tag{3}$$

2.1.2 The geometry model in point grinding process with NPGW

The grinding wheel axis inclines an angle α relative to the workpiece axis as shown in Fig. 3(a). To simplify the derivation with the existence of inclining angle α and consider the existence of angle θ, the workpiece with diameter d_{w} is equivalent to a virtual workpiece with $d_{\mathrm{w}}/\cos\theta$ and makes inclining angle α exist between workpiece axis and the grinding wheel axis, projected along with the vertical direction of grinding wheel axis as shown in Fig. 3(b).

So the equivalent diameter and the equivalent velocity of workpiece and grinding wheel in point grinding process with NPGW are,

$$\begin{cases} d_{we} = \dfrac{\left(d_w / \cos\alpha\cos\theta\right)^2}{d_w / \cos\theta} = \dfrac{d_w}{\cos^2\alpha\cos\theta} \\ d_{se} = d_s^2 / d_s \cos\theta = d_s / \cos\theta \end{cases} \tag{4}$$

$$\begin{cases} v_{we} = v_w \cos\alpha \\ v_{se} = v_s \end{cases} \tag{5}$$

where d_{we} and d_{se} are the equivalent diameters of the workpiece and grinding wheel in point grinding process with NPGW, v_{we} and v_{se} are the equivalent speed of the workpiece and grinding wheel in point grinding process with NPGW.

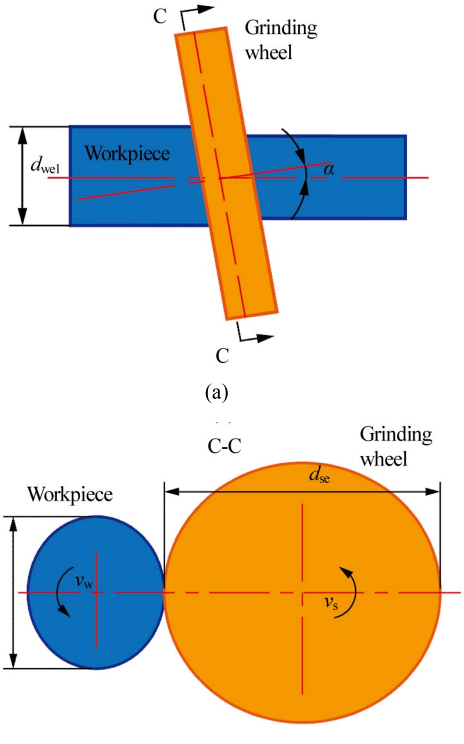

(a)

(b)

Fig. 3. Schematic of point grinding with NPGW.

The equivalent wheel diameter in point grinding process with NPGW is,

$$d_e = \frac{d_s d_w}{\cos\theta\left(d_s \cos^2\alpha + d_w\right)} . \tag{6}$$

The cutting path of the single grain is shown in Fig. 4(a). The shaded part represents the shape of the chip. The undeformed chip thickness is h_{m}. The cross-section of the undeformed chip is often triangular or rectangular. To simplify the calculation, the grinding chip is assumed to be triangular and the interference between single grain and workpiece can be obtained, as shown in Fig. 4(b). The maximum undeformed chip thickness h_{max} can be expressed as, in Refs. [13, 14].

$$h_{\max} = \left(\frac{3}{C\tan\gamma}\right)^{1/2}\left(\frac{v_{w,e}}{v_s}\right)^{1/2}\left(\frac{a_p}{d_e}\right)^{1/4} , \tag{7}$$

where C is the effective number of grains per unit area, γ is the half angle of grain top cone or indenter, a_p is the grinding depth.

According to the geometry relations in Ref. [3], the kinematic contact length of point grinding can be expressed as,

$$l_c = \left[\left(1 + \frac{v_{w,e}}{v_s}\right)^2 + \left(\frac{f_a n_w \cos\alpha}{60 v_s}\right)^2\right]^{\frac{1}{2}} \left(a_p \cdot d_e\right)^{\frac{1}{2}} . \tag{8}$$

The parameters above are introduced to the Eq. (8), the kinematic contact length of point grinding with NPGW is,

$$l = \sqrt{\left(1+\frac{v_w \cdot \cos\alpha}{v_s}\right)^2 + \left(\frac{f_a n_w \cos\alpha}{60 v_s}\right)^2} \times \sqrt{\frac{d_s \cdot d_w \cdot a_p}{\cos\theta(d_s \cos^2\alpha + d_w)}}\ , \tag{9}$$

where f_a is feed rate, n_w is the rotating speed of workpiece.

To simplify the calculation, assume that grains are spherical particles, have a diameter of d_g, and are uniformly distributed on the wheel. The volume fraction of grains is V_g. So, the number of grains per unit volume containing is [13],

$$N = \frac{6V_g}{\pi d_g^3}\ . \tag{10}$$

Let 1/4 volume effective grain be exposed to the wheel surface in average, and the exposed portion of each grain be only one effective cutting edge. So that, the number of effective cutting edge per unit area of grinding wheel surface is,

$$N_d = 4Nh, \tag{11}$$

where h is the cutting thickness.

Let the average cutting thickness of grains be $h_{max}/2$. The number of average effective cutting edge per unit area can be obtained as,

$$C = 2Nh_{max}. \tag{12}$$

Introducing Eq. (12) into Eq. (7), the maximum undeformed chip thickness is,

$$h_{max} = \left(\frac{3}{2N\tan\gamma}\right)^{1/3}\left(\frac{v_w \cdot \cos\alpha}{v_s}\right)^{1/3} \times \left(\frac{a_p \cos\theta\left(d_w + d_s\cos^2\alpha\right)}{d_s \cdot d_w}\right)^{1/6}. \tag{13}$$

2.1.3 The grinding force theoretical model of NPGW

In the actual grinding process, the grinding force consists of two parts, the chip deformation and the friction. The normal and tangential grinding force of a single grain F_{gn} and F_{gt} can be expressed as,

$$\begin{cases} F_{gn} = F_{gnc} + F_{gns} \\ F_{gt} = F_{gtc} + F_{gts} \end{cases} \tag{14}$$

where F_{gnc} is the normal force caused by chip deformation, F_{gns} is the normal force caused by friction, F_{gtc} is the tangential force caused by chip deformation, F_{gts} is the tangential force caused by frictions.

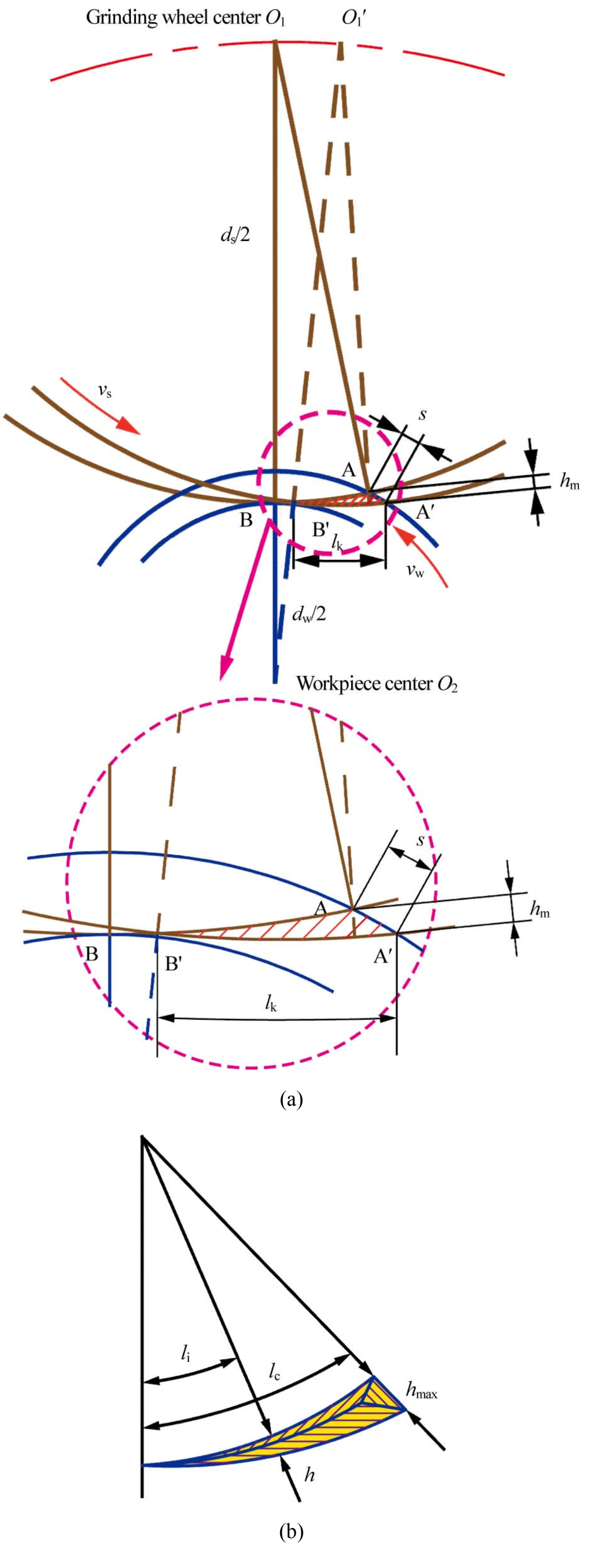

Fig. 4. Interference of single grain and workpiece material.

For single grain, F_{gns} is,

$$F_{gns} = \delta\bar{p}\ , \tag{15}$$

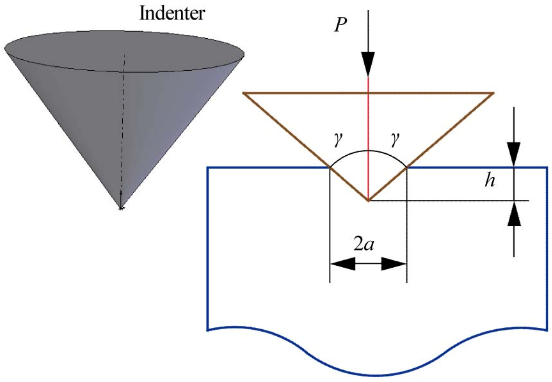

Fig. 5. Schematic of the grain indentation.

where δ is the actual contact zone of a single grain, $\bar{p}$ is the contact pressure between the wear plane and the workpiece.

F_{gts} can be expressed as,

$$F_{gts} = \mu\delta\bar{p}\,, \tag{16}$$

where μ is the friction coefficient between the workpiece and the wear plane.

According to Vickers hardness measurement theory and the feature size of indentation [13],

$$p = \xi Ha^2, \tag{17}$$

where p is the load, a is the indentation size, ξ is indenter geometry factor, for the Vickers indenter $\xi = 2$.

Fig. 5 shows the indentation feature size,

$$2a = 2h\tan\gamma. \tag{18}$$

In pure shear deformation conditions, F_{gnc} is expressed as,

$$F_{gnc} = \eta_0\xi\tan^2\gamma Hh^2\,, \tag{19}$$

where η_0 is a constant from 0 to 1.

In pure shear deformation conditions, F_{gtc} is expressed as,

$$F_{gtc} = \frac{\pi}{4\tan\gamma}\cdot F_{gnc} = \frac{\pi}{4}\eta_0\xi\tan\gamma Hh^2\,. \tag{20}$$

Thus the single grain normal grinding force F_{gn} and tangential grinding force F_{gt} are calculated as,

$$\begin{cases} F_{gn} = F_{gnc} + F_{gns} = \eta_0\xi\tan^2\gamma Hh^2 + \delta\bar{p} \\ F_{gt} = F_{gtc} + F_{gts} = \dfrac{\pi}{4}\eta_0\xi\tan\gamma Hh^2 + \mu\delta\bar{p} \end{cases} \tag{21}$$

According to geometry relationship in Fig. 4, $h \approx h_{\max}l_i/l$, replace the parameter h,

$$\begin{cases} F_{gn} = \eta_0\xi\tan^2\gamma H\left(\dfrac{h_{\max}}{l}l_i\right)^2 + \delta\bar{p} \\ F_{gt} = \dfrac{\pi}{4}\eta_0\xi\tan\gamma H\left(\dfrac{h_{\max}}{l}l_i\right)^2 + \mu\delta\bar{p}\,. \end{cases} \tag{22}$$

The normal grinding force and tangential grinding force per grinding width are equal to the sum normal force and tangential force of all effective grains per grinding width within the contact surface between workpiece and the grinding wheel,

$$\begin{cases} F_n' = \int_0^l F_{gn}N_d dl_i \\ F_t' = \int_0^l F_{gt}N_d dl_i\,. \end{cases} \tag{23}$$

The grinding force formula per grinding width of the grinding wheel and workpiece is,

$$\begin{cases} F_n' = \eta_0\xi\tan^2\gamma NHh_{\max}^3 l + 2N\delta\bar{p}h_{\max}l \\ F_t' = \dfrac{\pi}{4}\eta_0\xi\tan\gamma NHh_{\max}^3 l + 2\mu N\delta\bar{p}h_{\max}l\,. \end{cases} \tag{24}$$

2.2 The theory of grinding heat generation and distribution

Grinding heat is the heat generated by the consumption of grinding power during the grinding process and the heat transferred to the workpiece, grinding wheel, grinding chips, grinding coolant and emitted as stray radiation. Since each medium has a different thermal conductivity, most of the heat is passed to the workpiece [15, 16].

According to the heat distribution model developed by Rowe [9], the heat produced in grinding process can be mainly divided between four components: The grinding wheel, workpiece, chips, and coolant.

$$q_t = q_s + q_w + q_c + q_f\,, \tag{25}$$

where q_t, q_s, q_w, q_c and q_f are the total heat produced in grinding, and the heat transferred into the grinding wheel, workpiece, chips and coolant.

As shown in Fig. 6, the sum of the coefficients of each of the different transfer mediums is 1.

$$R_s + R_w + R_c + R_f = 1\,, \tag{26}$$

where R_s, R_w, R_c, R_f are the distribution coefficients of heat flux to the grinding wheel, workpiece, chips and coolant. In the case of dry grinding, R_f is the heat transfer coefficient of air, which can be converted to radiant heat.

It is necessary to define the heat flux of the moving heat source for the grinding temperature field, simulated by the finite element method. The triangular moving heat source model is adopted as shown in Fig. 7. The amplitude of the heat source decreases linearly in the opposite direction of mo-

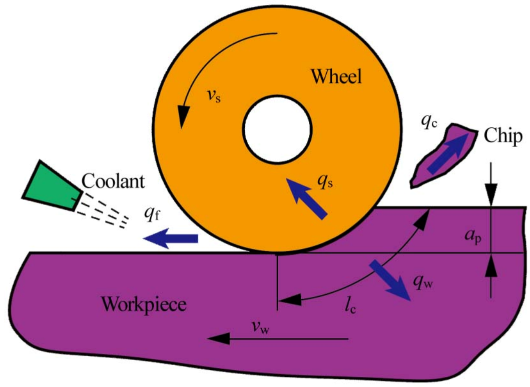

Fig. 6. Heat transfer model.

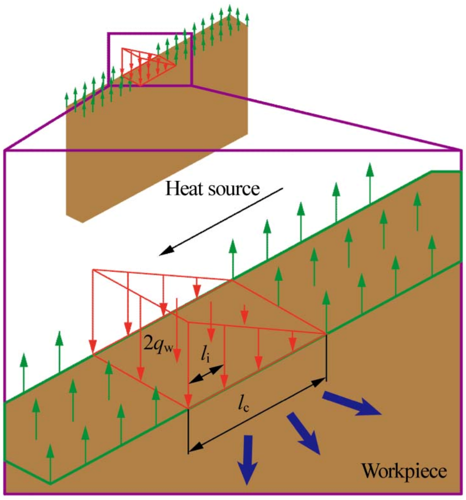

Fig. 7. Triangular heat source distribution model.

tion. Taking advantage of the finite element model, the temperature field distribution can be simulated, and the moving heat source is set according to the model assumptions. Depending on the program settings, the heat source moves forward in discrete steps of fixed step size l_i.

To calculate the heat generated in the contact zone, the power consumed during grinding is used. As such, the formula for calculating the total heat generated by the grinding wheel and workpiece can be given by,

$$q_t = \frac{P}{l_c b_w} = \frac{F_t v_s}{l_c b_w}, \tag{27}$$

where P is grinding power, b_w is the contact width between the grinding wheel and workpiece. The heat flow to each of the different media can be given as,

$$q_x = R_x q_t . \tag{28}$$

According to the apportion model of single grain sliding on the workpiece surface, for the heat flux taken away by the workpiece and the grinding wheel $q_{ws} = q_w + q_s$, the heat distribution ratio between the workpiece and grinding wheel R_{ws} can be obtained as,

$$R_{ws} = \frac{q_w}{q_w + q_s}\left(1 + \frac{0.974 k_g}{\beta_w \sqrt{r_0 v_s}}\right)^{-1}, \tag{29}$$

where k_g is the thermal conductivity of grain, r_0 is effective contact radius of grain, β_w is contact coefficient of the workpiece material.

3. Simulation of point grinding temperature field

3.1 Finite element modeling and simulation

During the grinding process, heat produced by point grinding is absorbed by the grinding wheel, workpiece, chips and coolant. Under different conditions, the proportion of the grinding heat transmitted to the workpiece will vary. The surface temperature of the workpiece can be analyzed by introducing α, which is used to build the new heat source model.

Mechanical energy can be transformed into thermal energy in the contact zone between the grains and material that is being removed. The heat flux can be calculated by,

$$q_t = \frac{P_w}{b_w l_c}, \tag{30}$$

where P_w is the grinding energy.

The heat flux in the contact zone changes due to the influence of inclining angle α. The heat flux transmitted to the workpiece can be described by

$$q_w = R_w q_t = \frac{R_w P_w}{l_c b_r} . \tag{31}$$

It can be seen that under the same grinding conditions, the heat flux of point grinding is different from traditional cylindrical grinding.

During the grinding process, heat transfer is a combination of the transient response and steady state response. The grains and workpiece produce heat via intermittent contact, and the heat generated in the transmission process will have a cumulative effect. Therefore, a numerical method can be used to simulate the process of heat flow and the temperature variation of the workpiece surface.

The triangular heat source distribution model was adopted since the cutting depth is small, enabling simplification of the model without losing accuracy. As shown in Fig. 8, the width of the heat source is equal to the grinding width, and the length of the distribution zone along the circumference of the workpiece is equal to the arc length of contact. The coordinates of any point A on the surface of the workpiece are (x_i, y_i), while O_1 and O_2 are the center of the grinding wheel and workpiece, respectively, and φ is the angle between O_1O_2 and

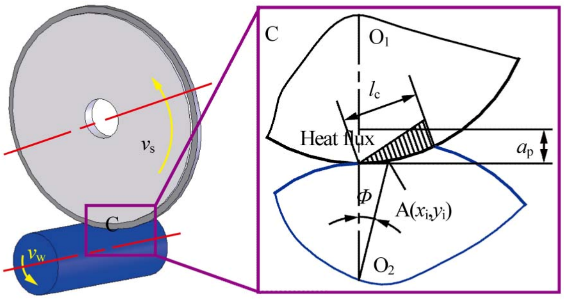

Fig. 8. Point grinding model.

O_2A. Since the cutting depth is much smaller than the radius of the workpiece, the influence of cutting depth in the geometrical model of the temperature distribution was not considered. The coordinate value of point A can be expressed by,

$$\begin{cases} x_i = \dfrac{d_w}{2}\sin\varphi \\ y_i = \dfrac{d_w}{2}\cos\varphi \end{cases} \tag{32}$$

where the angle φ can be expressed as,

$$\varphi = \frac{2v_w t}{d_w}. \tag{33}$$

The triangular surface heat source distribution field of the workpiece surface can be calculated using Eq. (33), and the maximum temperature will occur in a very short space of time, thereby affecting the workpiece surface. This should occur at the contact zone after the entire heat flow passes, that is, after the heat flow gradually decreases from the maximum value to the minimum value along the direction of the grinding movement. Therefore, to obtain the highest temperature value during grinding, the time required for the whole moving process can be calculated as,

$$t_c = \frac{l_c}{v_w}. \tag{34}$$

Projecting the triangular heat source onto the cylindrical surface of the workpiece is a complicated process. In particular the establishment of a moving heat source model along the circumferential direction is extremely complex. To simplify the model without affecting the simulation of the temperature field, the diameter of the shaft workpiece is set to infinity, and the model parameters are set according to the form of heat source in Fig. 7. The temperature simulation flow chart is shown in Fig. 9.

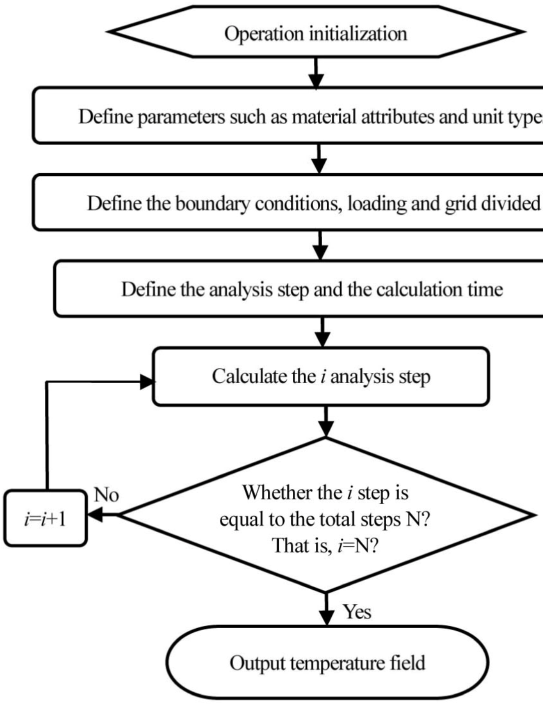

Fig. 9. Flow chart of simulation.

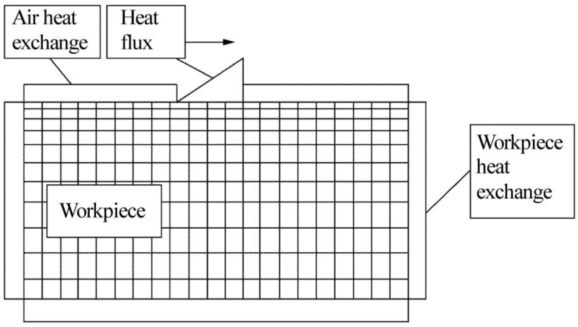

Fig. 10. Meshing and boundary definition of the model.

Based on the above conversion heat source model and ABAQUS software, a rectangular workpiece was chosen for the simulation. As such, a triangular heat source is applied to the workpiece surface, the displacement and speed of the movement are set according to the grinding direction, and in this study, QT700 is chosen as the material for the model. The grid can then be divided such that it is dense in the close range and loose at a distance and 8-node rectangular units are used. Furthermore, the grid can be determined by actual artifacts, which define the boundary conditions of the model, as shown in Fig. 10.

Grinding is a continuous process; therefore, to deal with the calculations the process must be discretized as a ‘time step and substep’. The heat source load repeatedly moves forward on the workpiece surface step by step. Then the entire grinding process can be obtained at any time step by moving the thermal load caused by the temperature change. To make the calculation more accurate and obtain satisfactory results, several calculations were carried out and compared; the load time step was taken as 0.002 s, and each time step was divided into three sub-steps.

Table 1. Material parameters.

Material parameters	QT700	CBN
Density ρ/(g/cm^3)	7.09	3.48
Elastic modulus E/GPa	169	71
Specific heat capacity/(J/kg·m^3)	481	500
Heat transfer rate/(W/m·K)	46.5	1300
Tensile strength σ/MPa	≥ 700	-
Elongation δ/(%)	≥ 2	-
Vickers-hardness Hv/HB	225~305	-
Poisson ratio v	0.305	-

According to the actual geometric topography of the model, the moving heat flux was loaded onto the surface of the model. A sufficient number of analytical steps was then set to obtain the maximum temperature and heat transfer of the contact zone, and the individual contact time was set to discrete. The contact zone is continuously heated by the heat source based on the previous heat transfer step. The initial temperature of the workpiece is set to the ambient temperature. Thermal properties of the material used in the simulation are shown in Table 1. The material of CBN is used only in the first four parameters in Table 1.

3.2 Simulation results and discussion

The temperature field distribution of the surface and subsurface near the grinding contact zone of the workpiece at 0.4 s under different grinding parameters is shown in Fig. 11. The inclining angle α of point grinding remained constant at 1°. During the simulation process two variables, grinding speed v_s and grinding depth a_p are set.

The grinding temperature in Fig. 11(c) is the highest, and in Fig. 11(b) the lowest. From Figs. 11(a) and (b), it can be seen that although the grinding speed increases, the maximum temperature in Fig. 11(b) is still lower than in Fig. 11(a), since the grinding depth decreases. So, the grinding depth a_p is the main factor affecting the temperature of the workpiece surface. When both the grinding speed and grinding depth are increased at the same time, the temperature is much higher in Fig. 11(c) than Fig. 11(a).

To study the effect of temperature on the subsurface quality of the workpiece, three points are taken along the same vertical direction, as shown in Fig. 11(a). These points are the workpiece surface D = 0 mm, below the surface D = 0.3 mm and D = 0.5 mm where D represents the depth of the point from the workpiece surface. The temperature of the three points varies with simulation time, as shown in Fig. 12. The temperature of the selected point moves along with the heat source on the workpiece surface, and first increases then decreases. The time taken for the temperature to reach the maximum value is delayed as depth increases. With the increase in depth, the maximum value reached by each point gradually decreases, and then each point tends to an identical temperature, indicating that the overall temperature of the workpiece after processing remains roughly the same.

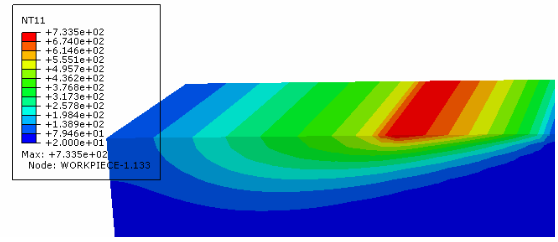

(a) v_s = 60 m/s, a_p = 0.1 mm

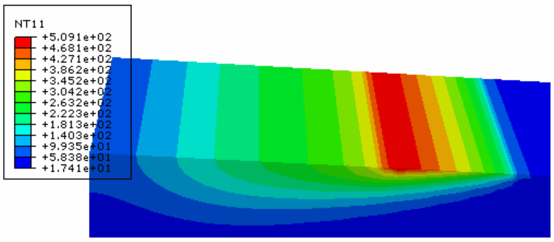

(b) v_s = 90 m/s, a_p = 0.05 mm

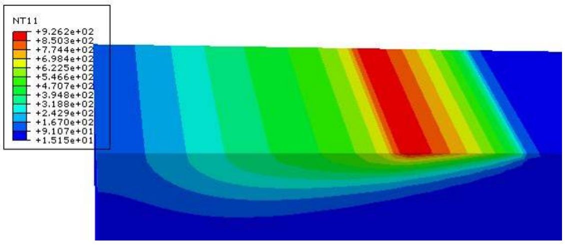

(c) v_s = 120 m/s, a_p = 0.2 mm

Fig. 11. Distribution of temperature field.

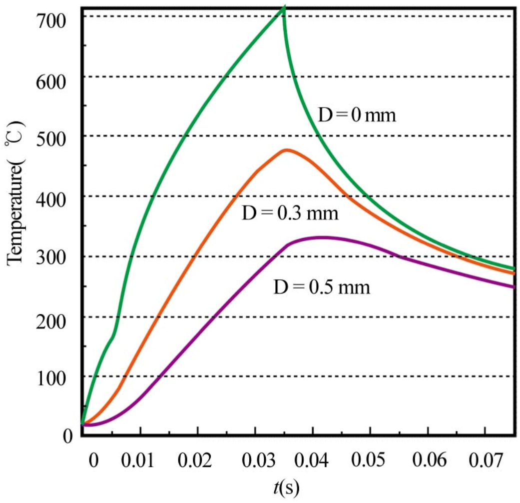

Fig. 12. Temperature versus time for different depths.

4. Experimental details

The NPGWs used in the experiments are made of CBN vitrified bond with coarse grinding zone angle θ. Select θ = 0°,

Table 2. The main parameters of NPGW.

External/inner diameter (mm)	Abrasive layer width/thickness (mm)	Coarse grinding zone angle θ	Abrasive grain size	Concentration
180/32	5/5	0°/4°/7°/10°/13°/16°/20°	120#	100 %

(a) Image of NPGWS (b) Magnified image of θ

Fig. 13. Image of NPGWS with coarse grinding zone angle θ.

4°, 7°, 10°, 13°, 16°, 20°. The grinding wheel with $\theta = 0°$ is the traditional point grinding wheel as a comparison test. Its coarse grinding zone width $X = 1.8$ mm, the precision grinding zone width $b = 3.2$ mm (Fig. 2). After setting the parameters X, b are fixed, only changing θ to fabricate seven NPGWs. The parameters of NPGW are shown in Table 2. The seven NPGWs fabricated are only different in coarse zone angle θ. The other parameters are the same. The grinding wheels manufactured are shown in Fig. 13(a), and a magnified image of the coarse grinding zone angle θ is shown in Fig. 13(b).

The strain gauge is used to measure grinding force. The core clamper of the grinder is processed four planes which are the same size and perpendicular to each other, at the neck of core clamper. And then the strain gauges are, respectively, pasted on the four planes. After calibration, the sensitivity of the force measurement core clamper in the vertical direction is 3.2 N/με and the sensitivity in the horizontal direction is 4.5 N/με. Experiments were conducted on MK9025A optical curve grinder, using seven fabricated NPGWs and QT700 stepped shaft workpiece with diameter $d_w = 55$ mm. The performance parameters of the material are shown in Table 1. The grinding parameters are adopted from Table 3 and grinding experiments are shown in Fig. 14.

Since the coordinate transformation is used to establish grinding force theoretical model, the measured grinding forces F_{nE} and F_{tE} need to be transformed to the grinding force at the contact zone F_n, F_t by the Eq. (35). Then F_n, F_t are divided by the width of wheel 5 mm. Thus, the grinding force of unit width is obtained, and contrasted them with the theoretical values F'_n, F'_t.

$$\begin{cases} F_n = \dfrac{F_{nE}}{\cos\theta} \\ F_t = \dfrac{F_{tE}}{\cos\alpha} \end{cases}. \tag{35}$$

Table 3. Experimental parameters.

No.	α(°)	θ(°)	a_p(mm)	v_f (mm/min)	v_s (m/s)
1	-1,-0.5,0, 0.5,1	0	0.03	1.2	45
2	0.5	0,4,7,10, 13,16,20	0.03	1.2	45
3	0.5	0	0.01,0.03, 0.05,0.065, 0.08	1.2	45
4	0.5	0	0.03	0.6,1.2, 1.8,2.4,3	45
5	0.5	0	0.03	1.2	35,40,45, 50,55,60

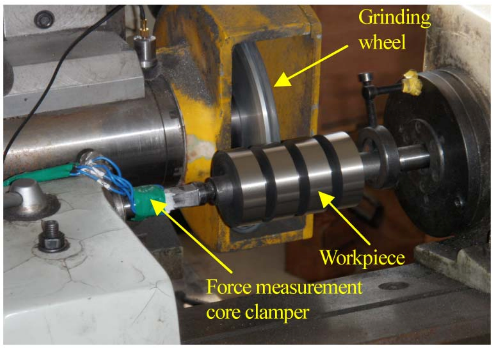

Fig. 14. Point grinding force experiment.

During the point grinding process, the grinding zone temperature characteristics include the short duration and high temperature gradient. A thermocouple is placed in the grinding zone to accurately measure the local temperature. While measuring the temperature, the wires may become winding due to the simultaneous rotation of the workpiece, which is an issue that must be solved.

The thermocouple is fixed with a clip-on structure, and the workpiece used in the thermocouple temperature test is shown in Fig. 15. Mica sheets with a thickness of 0.03 mm are used to provide insulation between the metal workpiece and thermocouple. A lock nut allows the sleeve to be clamped to the mandrel, and the clamping force secures the thermocouple in the slot. The ends of the constantan wire and Ni-Cr wire must always be in contact, and are insulated below the contact point, drawn out through the sleeve and slotted onto the shaft. The bushings and mandrel are also insulated with insulating sheets, and the pins of the respective thermocouple wires are connected to the two bushings. The outer circumference of the bushings are in contact with the two brushes, and avoid the thermocouple compensation wire as it is wound around the workpiece during the workpiece rotation. The two wires are connected to an amplifier, data acquisition card and PC in sequence to realize the data recording and display. Finally, the collected voltage signal is converted to temperature, according to the thermoelectric characteristics of the thermocouple. Since the thermocouple is not standard, it has to be calibrated

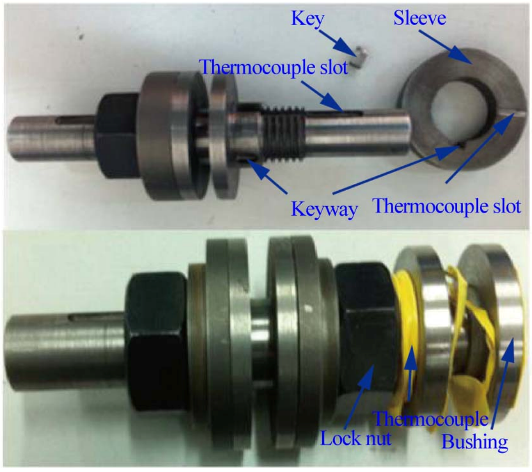

Fig. 15. Workpiece for thermocouple measurement.

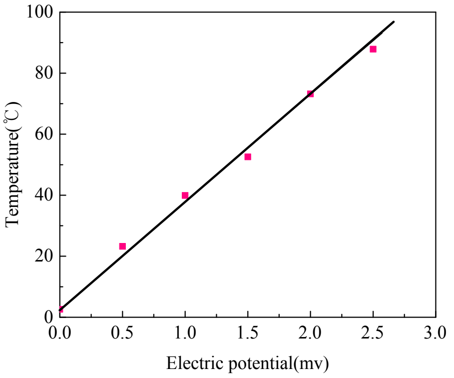

Fig. 16. Thermocouple calibration curve.

prior to temperature measurements in order to convert the collected voltage signal into a temperature value. The thermocouple calibration curve is presented in Fig. 16.

An MGR40P X-ray diffraction residual stress measurement instrument was also used in this experiment, with left and right X-ray detectors, as shown in Fig. 17. The X-ray target used for the diffraction crystal face is made of Cr palladium [2,1,1], and the angle is 156.41°, according to Bragg's law. During measurements, the ray tube swings along the orbit and can measure 7 different angles such that 2 detectors can collect data for up to 14 points. The curves were fitted by means of the ellipse method. The residual stress is measured from the surface to 6 different depths, along direction from the surface into the substrate, 0.1 mm, 0.25 mm, 0.5 mm, 0.75 mm and 1 mm. The depth is measured using the focal distance of the machine after polishing and acid corrosion. First, the residual stress is measured on the surface and then the surface of the corrosion layer is stripped by polishing and acid corrosion. Measurements are then taken at a distance of 0.1 mm from the surface, and so on, measuring the residual stress at all depth positions until the stress value of the last two groups are similar, thus tending toward stability. A negative measurement indicates compressive stress, a positive measurement indicates tensile stress, and the magnitude of stress is given by the absolute value.

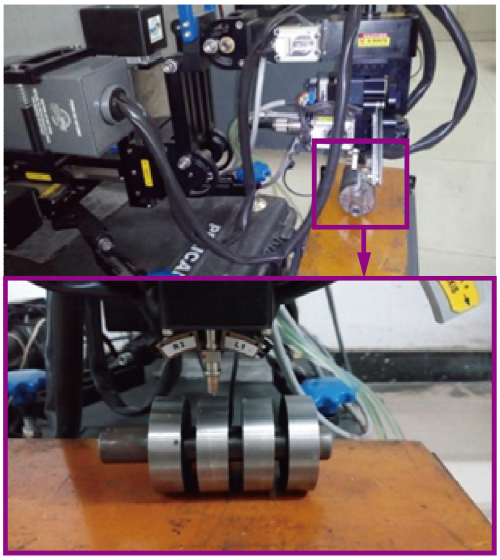

Fig. 17. Surface residual stress measurement system.

An $L_{16}(4^5)$ orthogonal experiment was conducted to investigate the influence of five factors – coarse grinding zone angle θ, inclining angle α, grinding depth a_p, axial feeding speed v_f, grinding wheel speed v_s on the grinding temperature. Single factor experiment was conducted to investigate the influence of each parameter on grinding force and verify the correctness of grinding force theoretical model and the simulation of grinding temperature. Plastic deformation is attributed to the production of compressive stress and grinding heat is attributed to the production of tensile stress. The coupling effect of grinding force and grinding temperature can be analyzed by researching residual stress of workpiece surface and subsurface.

5. Results and discussion

5.1 Grinding force

Fig. 18 shows the experimental measurements of seven wheels. The normal grinding force F_n and tangential grinding force F_t tend to decrease as the absolute value of the inclining angle α increasing, but with a lesser extent. All the curves are approximately symmetric about X = 0, so it is considered that $\pm\alpha$ has the same influence on the grinding force. Thus, point grinding process can reduce the grinding force. What's more, it can also be seen from the seven curves that when the NPGWs with larger θ, F_n and F_t are corresponding smaller. Especially, when $\theta = 0°$, the values of grinding force are maximum, and when $\theta = 20°$, the values are minimum.

Fig. 19 shows that the normal grinding force F_n and tangential grinding force F_t increase as the grinding depth a_p increasing. But both of them decrease as the coarse grinding zone angle θ increasing. Because when grinding depth a_p increases, the maximum undeformed chip thickness h_{max} increases, thereby the grinding force increases, which is coincided with

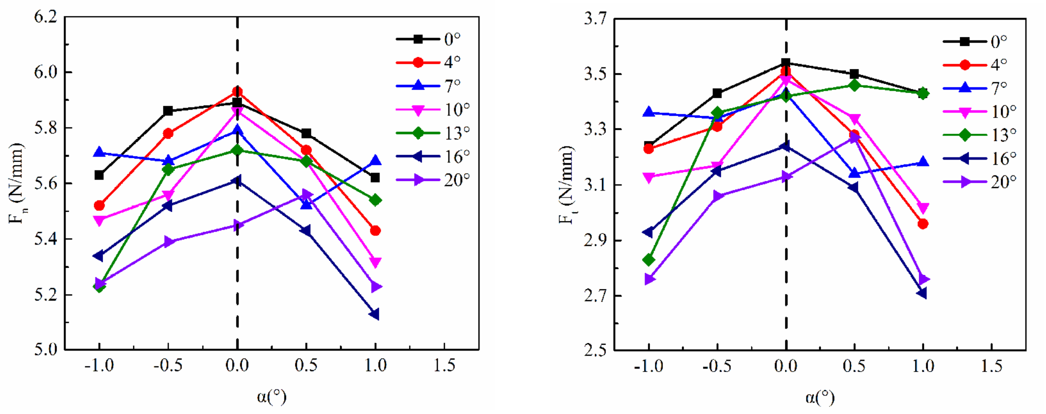

(a) (b)

Fig. 18. The effect of α on grinding force.

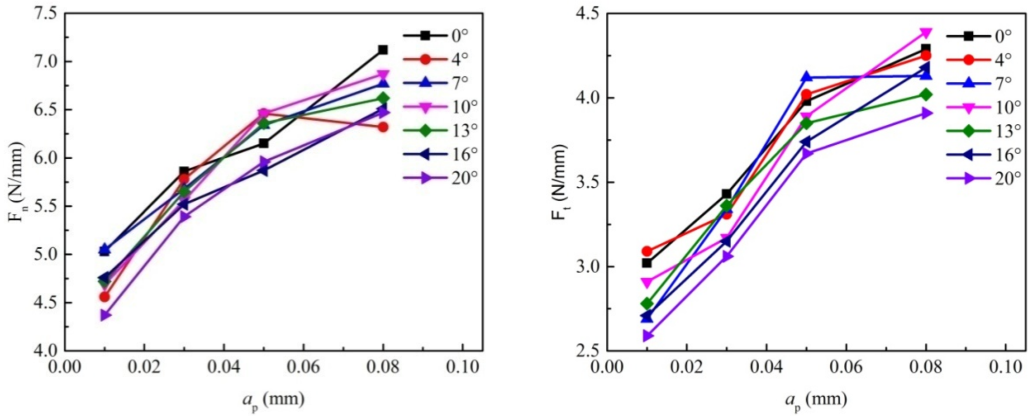

(a) (b)

Fig. 19. The effect of a_p on grinding force.

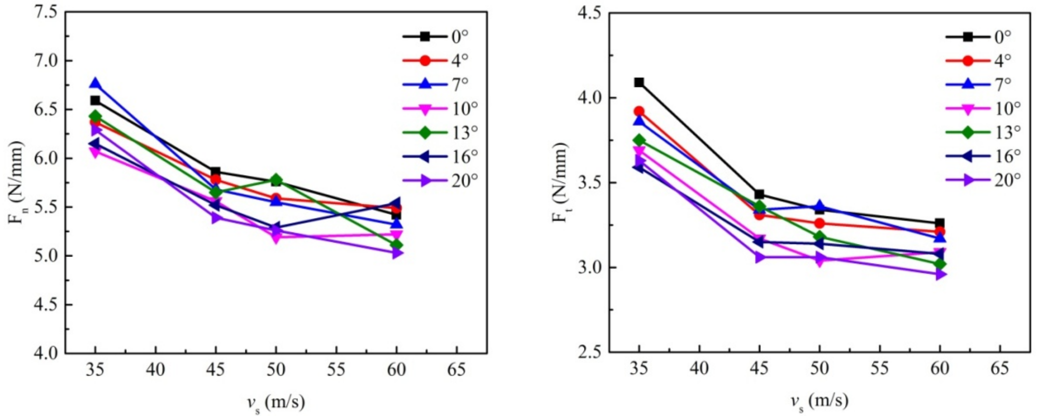

(a) (b)

Fig. 20. The effect of v_s on grinding force.

the theoretical model Eqs. (13) and (24).

Fig. 20 shows that the normal grinding force F_n and tangential grinding force F_t decrease as the wheel speed v_s increasing, and both of them decrease as the coarse grinding zone angle θ increasing. Because when the wheel speed v_s increases, the maximum undeformed chip thickness h_{max} decreases, thereby the grinding force decreases, which also coincides with the theoretical model.

There is another common phenomenon, both the theoretical values and experimental values, under the same grinding pa-

Table 4. Table of orthogonal experiments.

No.	Factors					
	α(°)	θ(°)	a_p(mm)	v_f(mm/min)	v_s(m/s)	Temperature (°C)
1	-1	0	0.01	0.6	35	251.69
2	-1	7	0.03	1.2	45	311.94
3	-1	13	0.05	1.8	50	293.62
4	-1	20	0.08	2.4	60	323.64
5	-0.5	0	0.03	1.8	60	388.53
6	-0.5	7	0.01	2.4	50	291.57
7	-0.5	13	0.08	0.6	45	301.77
8	-0.5	20	0.05	1.2	35	259.5
9	0.5	0	0.05	2.4	45	390.23
10	0.5	7	0.08	1.8	35	272.55
11	0.5	13	0.01	1.2	60	259.87
12	0.5	20	0.03	0.6	50	270.47
13	1	0	0.08	1.2	50	270.91
14	1	7	0.05	0.6	60	252.79
15	1	13	0.03	2.4	35	275.71
16	1	20	0.01	1.8	45	235.3
K1	1180.89	1301.36	1038.43	1076.72	1059.45	-
K2	1241.37	1128.85	1246.65	1102.22	1239.24	-
K3	1193.12	1130.97	1196.14	1190	1126.57	-
K4	1034.71	1088.91	1168.87	1281.15	1224.83	-
k1	295.22	325.34	259.61	269.18	264.86	-
k2	310.34	282.21	311.66	275.56	309.81	-
k3	298.28	282.74	299.03	297.5	281.64	-
k4	258.68	272.23	292.22	320.29	306.21	-
R	51.66	53.11	52.05	51.11	44.95	-
Influence degree			$\theta > a_p > \alpha > v_f > v_s$			
Optimal parameter combination			θ(20°), α(1°), a_p(0.01mm), v_f(0.6mm/min), v_s(35m/s)			

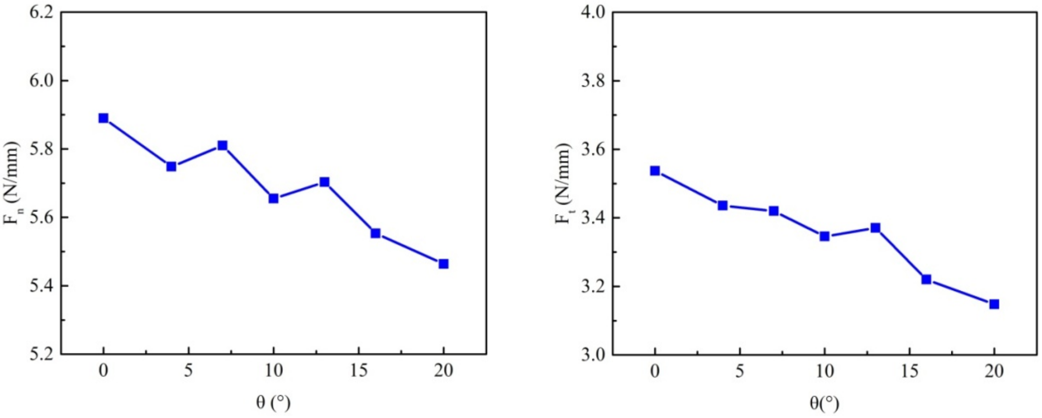

(a) (b)

Fig. 21. The effect of θ on grinding force.

rameters, the values of normal grinding force F_n are larger than those of the tangential grinding force F_t. This is because the grains of the grinding wheel have larger negative rake angle.

Furthermore, to compare the effects of different coarse grinding zone angle θ on grinding force, the arithmetic mean of the experimental data was calculated as the average grinding force. And then, we compared the average grinding force of every NPGW.

From Fig. 21, when $\theta = 0°$, the values of normal grinding force F_n and tangential grinding force F_t are the largest and when $\theta = 20°$, both F_n and F_t are smallest. Although there is a slight fluctuation, the overall trends of normal grinding force F_n and tangential grinding force F_t are the same. Both F_n and

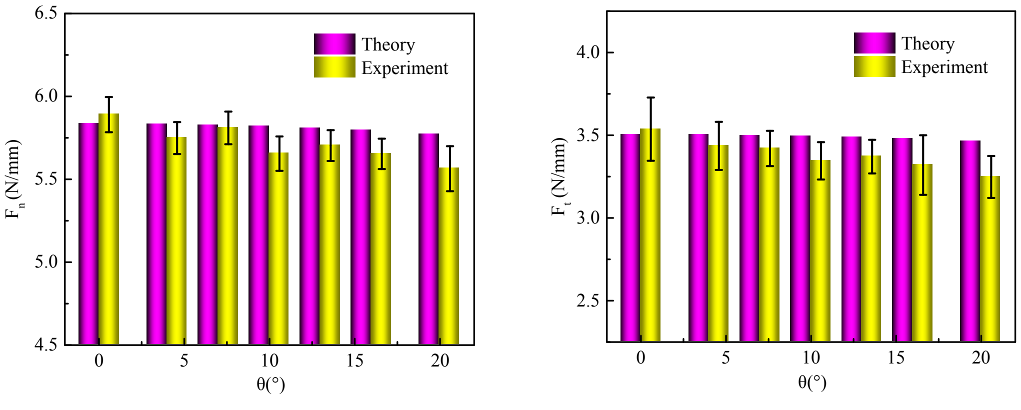

(a)

(b)

Fig. 22. Comparison of grinding force with different *θ*.

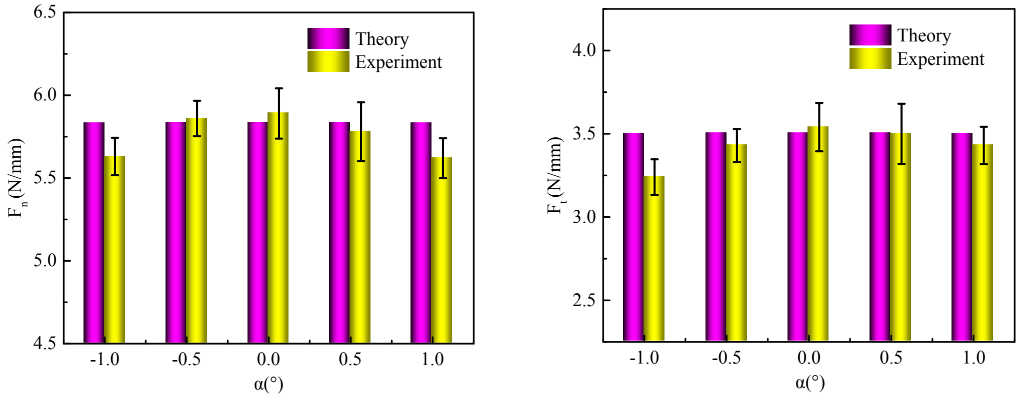

(a)

(b)

Fig. 23. Comparison of grinding force with different *α*.

F_t decrease as the coarse grinding zone angle θ increases. It means that the NPGW can decrease the grinding force.

5.2 Grinding temperature

Based on the data obtained in the orthogonal experiment shown in Table 4 and via the range analysis, primary and secondary orders of the degree of influence of each factor on the grinding temperature are obtained. The experimental results show horizontal changes in each factor affect the results differently. Greater range value R indicates a greater influence of each factor on the experimental results. The range values R, from Table 4, show that $R_\theta > R_{ap} > R_\alpha > R_{vf} > R_{vs}$, which suggests that the coarse grinding zone angle θ has the greatest influence on the grinding temperature, followed by the grinding depth a_p, inclining angle α, axial feeding speed v_f, and grinding wheel speed v_s. The grinding depth a_p has a greater influence on the grinding temperature than the grinding wheel speed v_s, which coincides with results obtained in the simulation. According to the calculated values of k, the minimum value of k can be selected for each factor such that the optimal parameter combination to reduce the grinding zone temperature is $\theta = 20°$, $\alpha = 1°$, $a_p = 0.01$ mm, $v_f = 0.6$ mm/min, $v_s = 35$ m/s.

5.3 Test verification of grinding force theoretical model

To verify the correctness of grinding force model of NPGW, the theoretical values and experimental results are compared, as shown in Figs. 22-25.

From all above figures, the trend of theoretical calculations coincides well with experimental measurements, and the values are close. Fig. 22 shows that the theoretical values and experimental values have the same trend and the grinding force decreases as the θ increases. From Fig. 23, both of the normal grinding force F_n and tangential grinding force F_t decrease as the absolute value of the inclining angle α increasing, and the curve of grinding force is symmetric on X = 0. When the inclining angle α is within the interval [-1, 1], it has a little effect on the grinding force. This coincides with the theoretical model. The theoretical formula contains only cosα, so the theoretical model has the same calculated values for $\pm\alpha$. In addition, due to the changing interval of inclining angle α is small, and the impact on the grinding force value is also small.

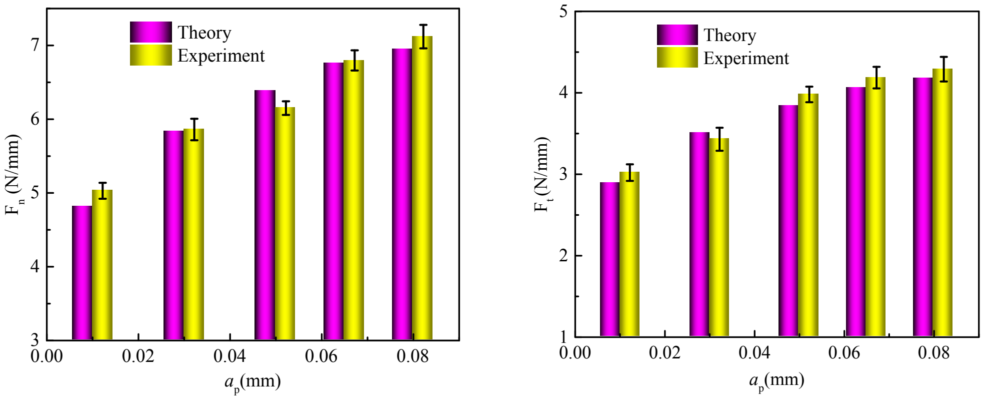

(a) (b)

Fig. 24. Comparison of grinding force with different a_p.

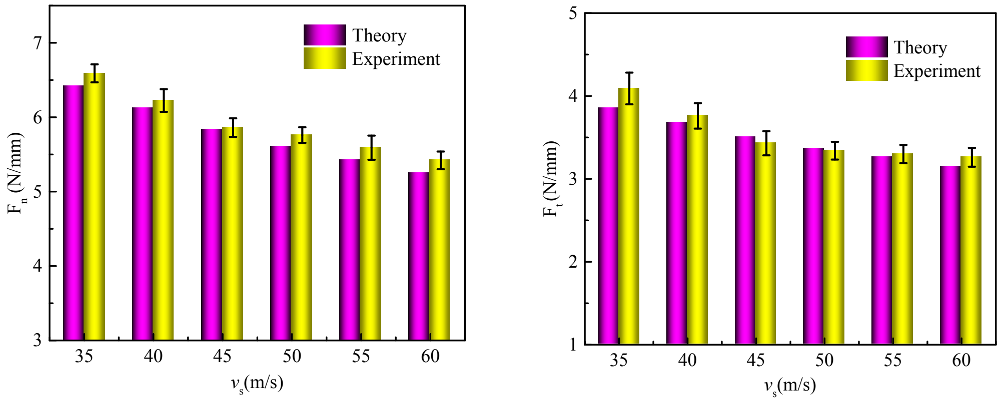

(a) (b)

Fig. 25. Comparison of grinding force with different v_s.

From Figs. 24 and 25, the theoretical values and experimental values are close and have the same trend, such that the normal grinding force F_n and tangential grinding force F_t increase as the grinding depth a_p increases, and F_n and F_t decrease as the wheel speed v_s increases.

5.4 Test verification of grinding temperature simulation

5.4.1 Influence of a_p on grinding temperature

It can be seen that the trends of temperature values of the simulation and experimental histograms are consistent, while the simulation results are larger than the actual measured from Fig. 26. The values of simulation are about 1.4 times of experiments. The reason is that the vibrations, the wear of grinding wheel and the thermocouple measurement errors are ignored in the simulation process.

In additional, the grinding temperature increases with increasing grinding depth a_p. Since a_p increases, the cutting depth of each grain increases, the arc length of contact also increases, the number of active grains involved in the grinding process increases; hence, the grinding power increases when the line speed remains unchanged, which thereby increases the grinding temperature.

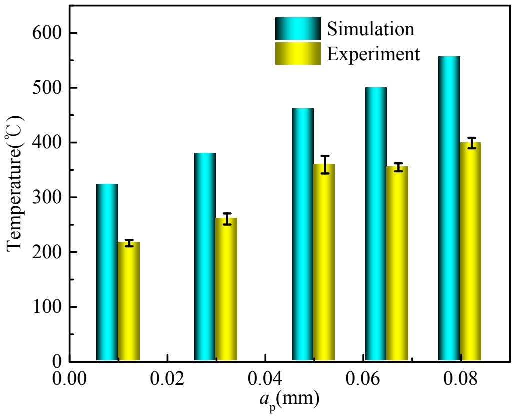

Fig. 26. Influence of a_p on grinding temperature.

5.4.2 Influence of v_f on grinding temperature

From the histogram (Fig. 27), the trends of temperature values of the simulation and experiment are also consistent, and the simulation results are still about 1.4-times of experiments.

In addition, the influence of the axial feeding speed v_f on grinding temperature is shown in Fig. 27. The grinding temperature increases with increasing v_f. As v_f increases, the

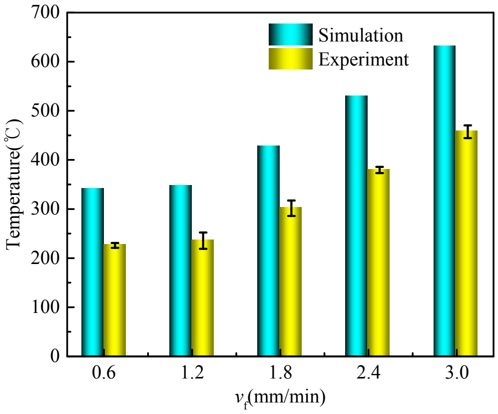

Fig. 27. Influence of v_f on grinding temperature.

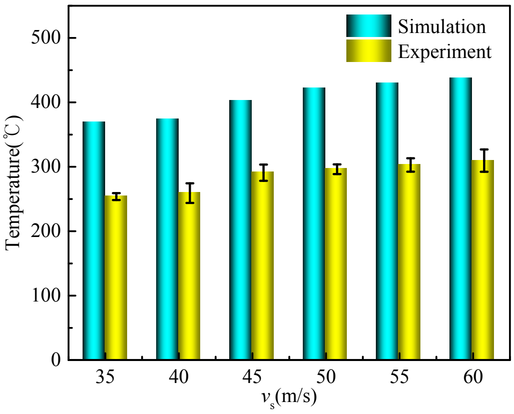

Fig. 28. Influence of v_s on grinding temperature.

grinding power also increases, the friction between grains and the workpiece increases, the heat source strength increases, and the grinding temperature therefore increases.

5.4.3 Influence of v_s on grinding temperature

From the histogram (Fig. 28), the trends of temperature values of the simulation are also coincided with experimental values. In addition, the grinding temperature increases with increasing grinding wheel. Since v_s increases, the number of grains involved in grinding also increases in unit time, and the plowing and sliding of the grains are intensified, which results in more heat thus raising the grinding temperature.

5.4.4 Influence of α on grinding temperature

From the histogram (Fig. 29), the trends of temperature values of the simulation also coincide with experimental values. In addition, the influence of the inclining angle α on the grinding temperature is approximately symmetrical about X = 0. Therefore, the sign of the inclining angle α is shown to have little influence on the grinding temperature, which mainly depends on the absolute value. The inclining angle α can reduce the grinding temperature, and the larger the absolute value of α, the lower the value of the grinding temperature.

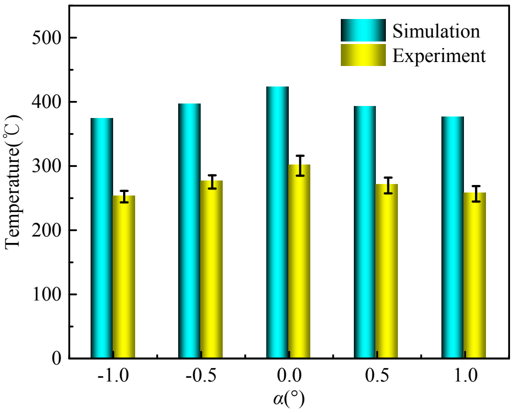

Fig. 29. Influence of α on grinding temperature.

The reason is that during the point grinding process the grinding wheel turns at the angle α relative to the workpiece. It results in a decrease in the size of the contact zone between the grinding wheel and workpiece, thus reducing the number of grains involved in grinding per unit time. The maximum undeformed chip thickness of a single grain decreases, thereby resulting in a reduction in heat generated during the grinding process. Furthermore, the existence of α is beneficial, as it improves the heat dissipation conditions. Within a certain range, a larger α can lead to better heat dissipation. For these reasons, the temperature in the point grinding process is lower than in traditional cylindrical grinding.

When coarse grinding zone angle θ varies from 0° to 20°, the temperatures are 275.3 °C, 261.6 °C, 256.2 °C, 255.8 °C, 249.5 °C, 246.7 °C, 241.6 °C, respectively. This means the grinding temperature decreases with increasing θ, which demonstrates that under the same conditions, θ leads to a decrease in the grinding temperature. This is due to the existence of θ, which allows the grinding chips to be more easily discharged from the grinding zone, thereby reducing the phenomenon of chips accumulation. Therefore, to a certain extent the heat generated during grinding is reduced, the heat dissipation conditions of the point grinding process are improved, and the heat generated during the grinding process can be better distributed. Moreover, the contact zone between the grinding wheel and workpiece becomes smaller, the grinding process is smoother, and the grinding temperature is decreased. In a word, the simulation provides an auxiliary and predictive method for the actual process and the NPGW can make the grinding zone temperature decreased.

5.5 Residual stress

During the grinding process, a large degree of plastic deformation of the metal occurs at the surface and subsurface level, and is considered cold plastic deformation. Along the direction of grinding, tensile deformation occurs at the workpiece surface, crystal grains are elongated, and the metal density decreases, such that specific volume increases. The material restricts deformation, thus producing residual compressive

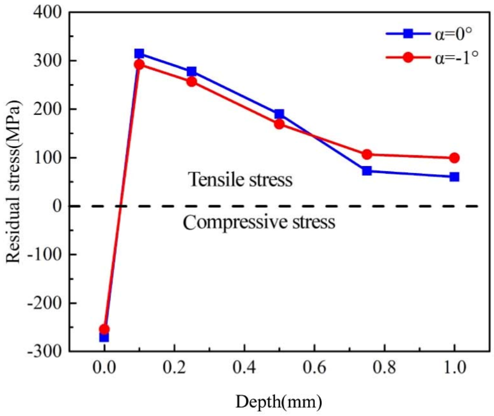

Fig. 30. Influence of α on residual stress of surface and subsurface.

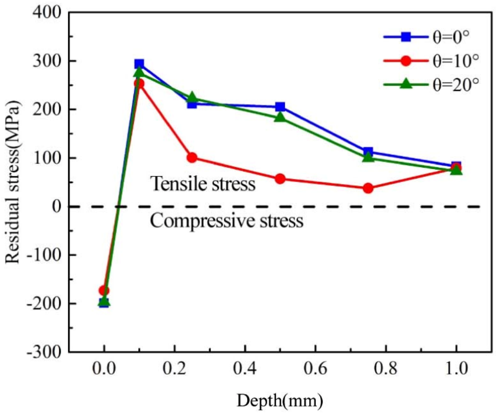

Fig. 31. Influence of θ on residual stress of surface and subsurface.

stress. Conversely, severe friction between the grains and the materials causes a large amount of heat to be generated in the grinding zone, which is then transmitted from the workpiece surface to the interior resulting in thermoplastic deformation. After the grinding process, the workpiece is cooled to ambient temperature, and the volume of material retracts. The workpiece surface is subjected to thermal plastic deformation, volume expansion, and shrinkage, resulting in the generation of tensile stress. Residual stress is also generated as a result of the superposition of various influencing factors. When plastic deformation plays a major role, the residual stress can be expressed as compressive stress. In contrast, when the influence of the grinding heat plays a major role, the residual stress is expressed as tensile stress.

5.5.1 Influence of α on residual stress

In Fig. 30, the machined workpiece surface produces compressive stress, indicating plastic deformation played a major role. When α = -1°, compressive stress on the workpiece surface is lower than when α = 0°. This is because the grinding wheel and workpiece are changed to a point contact when α = -1°, thereby reducing the contact area and the effects of plastic deformation, which coincides with the results of grinding force.

Also from Fig. 30. the compressive stress gradually decreases and the tensile stress gradually increases in the superficial subsurface region, as the compressive stress gradually changes to tensile stress, indicating grinding heat plays a major role. The tensile stress reaches a maximum value at 0.1 mm below the surface. With a further increase in depth, the tensile stress gradually decreases to the substrate value. The maximum tensile stress of the workpiece subsurface when α = -1° is lower than when α = 0°. Because it is beneficial to reduce the grinding heat generation and improve the heat dissipation conditions when α = -1° which coincides with the results of grinding temperature. Hence, the effect of the grinding heat is reduced when α = -1° compared with α = 0°, which results in the decrease of the tensile stress. In general, the point grinding process can reduce the residual stress, including the compressive stress and tensile stress. And the inclination angle α has little effect on the residual stress of the surface and subsurface because the two curves are close for the same range.

5.5.2 Influence of θ on residual stress

As can be seen from Fig. 31, compressive stress is generated on the workpiece surface, which helps to suppress the generation of cracks. The residual stress on the workpiece surface when θ = 10° is less than θ = 0°, because as θ increases, the grinding force decreases, the extrusion force decreases, and plastic deformation decreases, which results in a decrease in residual stress. However, with increasing θ, the grinding heat rapidly decreases and the extent of this decrease is greater. So, the combined effects of the two factors lead to an increase in the residual compressive stress value. Thus, when θ = 20°, the residual stress on the workpiece surface is greater than θ = 10°. In summary, the NPGW reduces residual stress on the workpiece surface, and the grinding wheel with θ = 10° results in the greatest reduction. Compared to the conventional point grinding wheel, the NPGW reduces the residual stress by 12 %.

The compressive stress changes to tensile stress with increasing depth (Fig. 31). Moreover, the tensile stress reaches a maximum value at 0.1 mm below the surface. With further increasing depth, the tensile stress decreases gradually. The maximum value of tensile stress of the workpiece subsurface is largest when θ = 0°. This is because the grinding temperature is highest when θ = 0°, hence the tensile stress is also largest. According to the above analyses, the NPGW reduces the residual stress of surface and subsurface, including the compressive stress and tensile stress.

5.5.3 Influence of a_p on residual stress

As seen from Fig. 32, when a_p = 0.03 mm and a_p = 0.05 mm, compressive stress is generated on the workpiece surface. The residual compressive stress decreases with increasing grinding depth a_p. When a_p = 0.08 mm, tensile stress is generated on the workpiece surface, since when a_p is small,

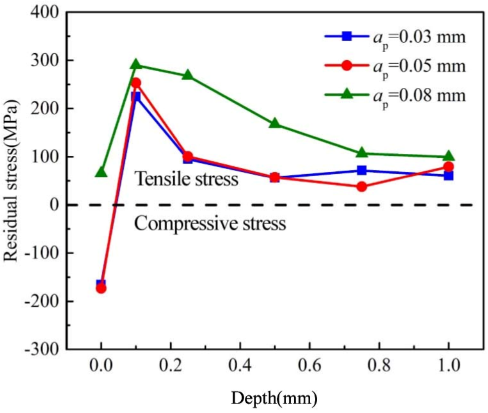

Fig. 32. Influence of a_p on residual stress of surface and subsurface.

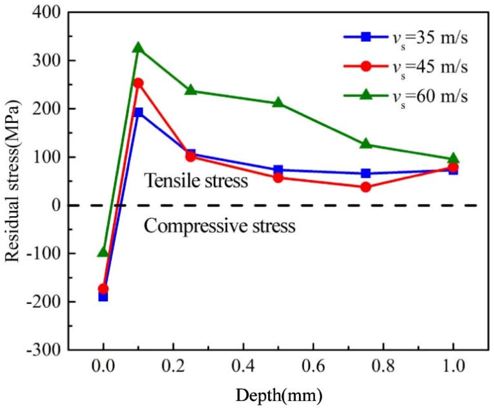

Fig. 33. Influence of v_s on residual stress of surface and subsurface.

the grinding temperature is low and plastic deformation mainly occurs on the metal surface, so stress on the grinding surface is compressive. However when a_p is large, the average undeformed chip thickness of single grain increases, the grinding temperature increases, the proportion of grinding heat increases playing a major role, and stress is expressed in the form of residual tensile stress.

Also, the compressive stress changes to tensile stress with increasing depth. The tensile stress reaches a maximum value at 0.1 mm below the surface. When a_p = 0.08 mm, the tensile stress is largest at 289.7 MPa. The maximum tensile stresses when a_p = 0.05 mm and a_p = 0.03 mm are 253.3 MPa and 224.5 MPa, respectively. Then, along the depth direction, the residual tensile stress gradually decreases. In conclusion, if the residual stress of the machined workpiece surface is taken as the main quality index, a smaller grinding depth a_p is recommended. However, decreasing the grinding depth will lead to lower grinding efficiency. Therefore, the influence of other factors should also be taken into account in the actual grinding process.

5.5.4 Influence of v_s on residual stress

From Fig. 33, the stress produced on the grinding surface is residual compressive stress. The residual compressive stress decreases as the grinding wheel speed v_s increases. This is due to the effect of grinding heat, which has influence less than the mechanical load, so the stress manifests as compressive stress. With increasing grinding wheel speed v_s, the grinding force decreases and the effect of plastic deformation decreases. Furthermore, as the number of grains involved in grinding per unit time increases, the grinding temperature increases and the proportional effect of the grinding heat increases, such that the compressive stress is gradually reduced and tensile stress gradually increases. Therefore, the following experimental results are explained: The maximum tensile stress is 324.7 MPa when v_s = 60 m/s; the maximum tensile stresses when v_s = 35 m/s and v_s = 45 m/s are 192.5 MPa and 253.3 MPa, respectively. The tensile stress reaches the maximum value at 0.1 mm below the surface and the residual tensile stress is gradually reduced.

In general, the residual stress is affected by the grinding force and the grinding temperature coupled. The stress on the machined workpiece surface is compressive, indicating that grinding force plays a major role. Due to the existence of compressive stress, the workpiece surface is not easy to crack; however, below the workpiece surface at a superficial position, there is still tensile stress, indicating that grinding heat plays a major role and a risk of generating cracks.

6. Conclusion

The calculated values of grinding force theoretical model of NPGW coincided with the experimental measurements. The grinding zone temperature can be simulated by using the finite element method, and the simulation results were verified by experiments. Thereby, the theoretical model and simulation provide an auxiliary and predictive method for an actual process.

The NPGW and point grinding process can reduce the grinding force and the grinding zone temperature. In addition, the grinding force would increase as the grinding depth a_p increasing and decrease as the wheel speed v_s is increasing. The grinding zone temperature increases with increasing grinding depth a_p, axial feeding speed v_f and grinding wheel speed v_s.

Through $L_{16}(4^5)$ orthogonal experiment, the primary and secondary factors affecting grinding zone temperature are as follows: coarse grinding area angle θ > grinding depth a_p > inclining angle α > feed speed v_f > wheel speed v_s. The optimum parameter combinations to reduce the grinding temperature were determined to be $\theta = 20°$, $\alpha = 1°$, $a_p = 0.01$ mm, v_f = 0.6 mm/min, v_s = 35 m/s.

Stress on the grinding workpiece surface is mainly compressive, which shows that plastic deformation plays a major role, and the subsurface compressive stress is gradually transformed into tensile stress, which shows that the grinding heat plays a major role with increasing depth. The tensile stress reaches a maximum value at 0.1 mm below the surface, and further decreases with increasing depth. On the workpiece surface, the effect of grinding force is greater than grinding temperature, while on subsurface, the effect of grinding temperature is greater than grinding force. The NPGW and point grinding process can reduce the residual stress of workpiece surface and subsurface, in the case of tensile and compressive stress. Finally, the residual stress on the workpiece surface decreases, and the maximum tensile stress of the subsurface increases as the grinding depth a_p and the grinding wheel speed v_s is increasing.

Acknowledgments

The authors would like to thank the National Natural Science Foundation of China (No. 51705069), the Fundamental Research Funds for the Central Universities (N160303002) and National Natural Science Foundation of China (No. 51775100).

References

[1] Y. D. Gong, Y. M. Liu, J. Qiu and T. C. Han, Research on simulation and experiment for workpiece micro-surface in point grinding, *J. of Mechanical Engineering*, 48 (17) (2012) 165-171.

[2] G. Q. Yin, Y. D. Gong, C. Wang and X. L. Wen, Effects of processing parameters for novel point grinding wheels on surface quality, *J. of Northeastern University (Natural Science)*, 35 (2) (2014) 273-276.

[3] G. Q. Yin, Y. D. Gong, X. L. Wen, Y. K. Zhang and J. Cheng, Modeling and experimental investigations on point grinding force for novel point grinding wheel, *J. of Mechanical Engineering*, 52 (9) (2016) 193-200.

[4] J. A. Badger and A. A. Torrance, A comparison of two models to predict grinding forces from wheel surface topography, *International J. of Machine Tools & Manufacture*, 40 (8) (2000) 1099-1120.

[5] R. L. Hecker, S. Y. Liang, X. J. Wu, P. Xia and D. G. W. Jin, Grinding force and power modeling based on chip thickness analysis, *International J. of Advanced Manufacturing Technology*, 33 (5-6) (2004) 449-459.

[6] S. Malkin, *Grinding technology theory and application of machining with abrasive*, Translated by G. Q. Cai, Y. D. Gong, G. L. Song, Northeastern University Press, Shen Yang, China (2002).

[7] J. L. Gonzalez-Santander and G. Martin, A theorem for finding maximum temperature in wet grinding, *Mathematical Problems in Engineering*, 2015 (10) (2015) 1-13.

[8] P. V. Vinay and C. S. Rao, Temperature assessment in surface grinding of tool steels, *J. of Mechanical Science and Technology*, 29 (11) (2015) 4923-4932.

[9] W. B. Rowe, Thermal analysis of high efficiency deep grinding, *International J. of Machine Tools & Manufacture*, 41 (1) (2001) 1-19.

[10] X. C. Huang, D. H. Zhang, C. F. Yao and J. X. Ren, Effects of grinding parameters on surface integrity of GH4169 nickel-based superalloy, *J. of Aerospace Power*, 28 (3) (2013) 621-628.

[11] Y. Z. Sun, H. T. Liu and Z. S. Lu, Finite element simulation and experimental research of residual stresses in the cutting based on the coupled thermo-mechanical model, *J. of Mechanical Engineering*, 47 (1) (2011) 187.

[12] Y. D. Gong, G. Q. Yin, X. L. Wen, M. Han, J. B. Yan and J. Cheng, Research on simulation and experiment for surface topography machined by a novel point grinding wheel, *J. of Mechanical Science and Technology*, 29 (10) (2015) 4367-4378.

[13] G. Z. Xie, Z. T. Shang, X. M. Sheng, Y. Wu and J. W. Yu, Grinding force modeling for high-speed deep grinding of engineering ceramics, *J. of Mechanical Engineering*, 47 (11) (2011) 169-176.

[14] G. Z. Xie, H. W. Huang, H. Huang, X. M. Sheng, H. Q. Mi and W. L. Xiong, The experimental investigations of advanced ceramics in high efficiency deep grinding, *Chinese J. of Mechanical Engineering*, 43 (1) (2007) 176-184.

[15] M. Gostimirovic, V. Pucovsky, P. Kovac, M. Sekulic and B. Savkovic, An analytical study of energy partition in grinding, *Key Engineering Materials*, 686 (2016) 80-85.

[16] X. M. Huang, Y. H. Ren, B. Zheng, Z. H. Deng and Z. X. Zhou, Experiment research on grid-hardening of AISI5140 steel based on thermal compensation, *J. of Mechanical Science and Technology*, 30 (8) (2016) 3819-3827.

Yin Guoqiang is currently a lecturer at Northeastern University, China. His research interests include grinding and precision machining.

Gong Yadong is currently a Professor and a Ph.D. candidate supervisor at Northeastern University, China. His main research interests include grinding and precision machining, digital manufacturing, micro precision process.